How water, temperature and seismicity control the preparation of massive rock slope failure (Hochvogel, DE/AT)

Johannes Leinauer[1], Michael Dietze[2,3], Sibylle Knapp[1,4], Riccardo Scandroglio[1], Maximilian Jokel[1], and Michael Krautblatter[1]

[1]Technical University of Munich, TUM School of Engineering and Design, Landslide Research Group, München, Germany
[2]Georg-August-Universität Göttingen, Faculty of Geosciences and Geography, Göttingen, Germany
[3]GFZ German Research Centre for Geosciences, Potsdam, Germany
[4]UNESCO Global Geopark Swabian Alb, Schelklingen, Germany

Correspondence: Johannes Leinauer (johannes.leinauer@tum.de)

Abstract. The increasing hazard of major rock slope failures, exacerbated by climate change, underscores the importance of anticipating pre-failure process dynamics. While standard triggers are recognized for small rockfalls, few comprehensive driver quantifications exist for massive pre-failure rock slopes. Here we exploit >4 years multi-method high-resolution monitoring data from a well-prepared high-magnitude rock slope instability. To quantify and understand the effect of possible drivers - water from rain and snowmelt, internal rock fracturing and earthquakes - we correlate slope displacements with environmental data, local seismic recordings and earthquake catalogues. During the snowmelt phase, displacements are controlled by meltwater infiltration with high correlation and a time lag of 4-9 days. During the snow-free summer, rainfall drives the system with a time lag of 1-16 h for up to several days without a minimum activation rain sum threshold. Detected rock fracturing, linked to temperature and freeze-thaw cycles, is predominantly surface-near and unrelated to displacement rates. A classic Newmark analysis of recent and historic earthquakes indicates a low potential for immediate triggering of a major failure at the case site, unless it is already very close to failure. Seismic topographic amplification of the peak ground velocity at the summit ranges from a factor of 2-11 and is spatially heterogeneous, indicating a high criticality of the slope. The presented methodological approach enables a comprehensive rockfall driver evaluation and indicates where future climatic changes, e.g. in precipitation intensity and frequency, may alter the preparation of major rock slope failures.

1 Introduction

Massive rock slope failures are an important geomorphic hazard that causes increasing risk in the wake of climate change and population growth (Lacasse and Nadim, 2009; Picarelli et al., 2021). To prevent damage to people or property, the anticipation of such events becomes highly crucial (Sättele et al., 2016; Chae et al., 2017; Pecoraro et al., 2019; Leinauer et al., 2023), and thus, relevant drivers and potential triggers of imminent failures must be identified and understood. Exploiting the available data of comprehensive monitoring and early warning systems to gain understanding of all relevant pre-failure process dynamics should therefore become a standard procedure (Gischig et al., 2016). However, while standard and qualitative rock fall

triggering factors are known, site-specific quantifications of the relevant drivers of high-magnitude rock instabilities based on monitoring data are often missing.

Rockfall release can be caused by a reduction of resisting forces and/or an increase of driving forces. In the preparation phase,
25 promoting drivers act on a rock slope over months to millions of years (Dietze et al., 2017b) bringing the system progressively closer towards critical slope stability (Oswald et al., 2021). This is achieved by the development of a sliding plane over different time scales, e.g. through seasonal pore pressure increase (Preisig et al., 2016), repeated seismic loading (Gischig et al., 2016), or long-term fracture propagation following weathering and erosion, glacial debuttressing (Eberhardt et al., 2004; Ballantyne et al., 2014) or permafrost degradation (Hilger et al., 2021). Imminently before failure, a trigger acts on the balance between
30 stabilising forces and stress leading to unstable conditions initiating rockfall within short time (Wieczorek, 1996). Of course, promoting drivers in the preparation phase and triggering factors terminating this phase can overlap and interact, and the transition between the two may be gradual. In some cases the progressive weakening of material could lead to slope failure without an apparent external trigger (Lagarde et al., 2023) but in such state, the rock slope instability becomes increasingly sensitive to external drivers. However, a detailed and comprehensive knowledge of how and how much internal and external
35 drivers control the pre-failure stage of imminent rock slope failures is missing at most sites, but crucial for anticipation tasks.

Possible rockfall drivers and triggers (Fig. 1) include (e.g. Stock et al., 2013; Dietze et al., 2017b) (a) rainfall, (b) snowmelt, (c) rock fracturing and crack propagation, (d) earthquakes, (e) temperature gradients, (f) freeze-thaw-cycles, (g) wind, (h) lightning, (i) rock or ice fall inducing secondary rockfall, (j) snow or rock avalanches, (k) volcanic activity, (l) vegetation growth and root prying, (m) permafrost degradation (Krautblatter et al., 2013), and (n) human or animal activity. The significance of some
40 of these factors might change in the future due to climatic shifts, e.g. precipitation frequency and severity or temperature (IPCC, 2019).

Heavy precipitation and rapid snowmelt are documented to be amongst the most important drivers for rockslides across the globe (e.g. Wieczorek, 1996; Helmstetter and Garambois, 2010; Stock et al., 2013; LaHusen et al., 2020). Infiltrating water can destabilize rock slopes repeatedly in short time scales by building significant hydrostatic pressure in clefts, elimination of
45 the joint cohesion, lowering of the joint friction angle and reduction of the effective normal stress at the sliding surface due to uplift (Erismann and Abele, 2001; Wyllie and Mah, 2004; Scandroglio et al., 2021). Additionally, long-term hydro-mechanical loading cycles are proven to have a promoting effect in deep-seated landslides (Gischig et al., 2016). Constraining the amount of water, respectively the pore pressure inside a rock slope, is challenging without the availability of boreholes. In such cases, the direct measurement of the water supply via rain gauges or snow stations is easier to obtain.

50 Progressive crack propagation in fracturing rock is one of the main internal drivers of rock slope failures (Petley, 2004; Lagarde et al., 2023). Critical and subcritical crack growth along active sliding planes intensifies the stress concentration at the crack tips (e.g. Amitrano and Helmstetter, 2006; Voigtländer et al., 2018), as with every failing rock bridge, the stress increases at the remaining rock bridges (Kemeny, 2003). Once most rock bridges have been degraded, episodic deformation release might be controlled by macro-roughness creating obstacles along the sliding plane (Borri-Brunetto et al., 2004; Dietze
55 et al., 2021). Stress release in the form of rock fracturing generates typical and distinguishable seismic signals that can be recorded with local seismic networks (Senfaute et al., 2009; Helmstetter and Garambois, 2010; Hibert et al., 2011; Provost
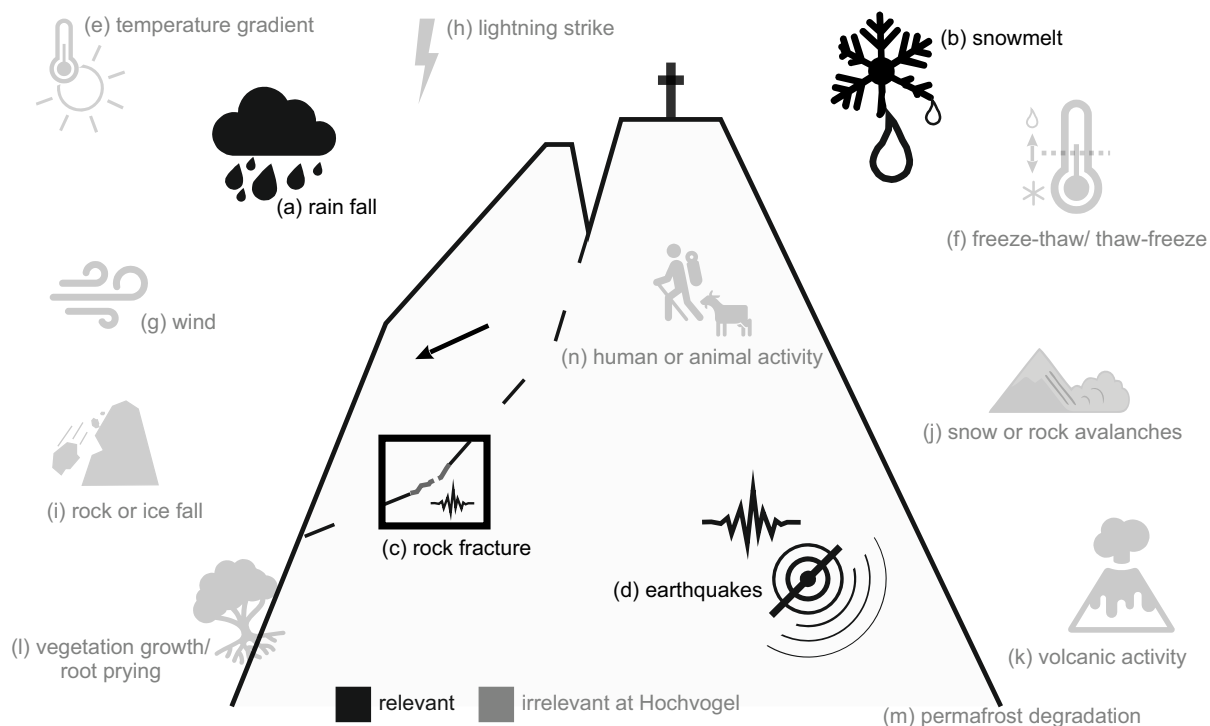
Figure 1. Factors that can potentially promote and/or trigger rockfalls. Black processes (a-d) are relevant for a major failure at our case site Hochvogel, grey ones (e-n) can be excluded due to the reasons in the text.

et al., 2017; Dietze et al., 2021; Lagarde et al., 2023). Isolating the episodically occurring short events within the large datasets is challenging with manual techniques and thus, established machine learning procedures can help to build a database of rock fracturing events (Provost et al., 2017; Hibert et al., 2017; Wenner et al., 2021; Langet and Silverberg, 2023).

60   Earthquakes frequently trigger numerous landslides (e.g. Wieczorek, 1996; Jibson et al., 2006; Meunier et al., 2007; LaHusen et al., 2020; Marc et al., 2016; Massey et al., 2022). Prehistorically, they seem to have played a significant role in preparing and triggering large rockslides due to the spatio-temporal coincidence of major earthquakes and rock slope failures (Knapp et al., 2018; Oswald et al., 2021). The correlation of landslide occurrence and volume with peak ground acceleration (PGA) values (Meunier et al., 2007; Massey et al., 2022) reinforces the destabilizing nature of strong seismic waves, but recurring

65   earthquakes are further a promoting factor due to seismic fatigue (Gischig et al., 2016; Oswald et al., 2021). Earthquake waves add additional stress to a slope instability by accelerating the ground with a specific amount of energy for a limited time depending on frequency and direction. This ground motion can be measured directly at an instrumented instability with the same local seismometers that also record rock fracturing. If direct observations at the site of interest are not available, theoretical block displacements can be estimated with the well-known Newmark analysis (Newmark, 1965). This method

70   allows to evaluate a great number of historic earthquakes from earthquake catalogues or systematic parameter sets towards

their triggering potential and deformational influence. In steep topography it is furthermore important to consider frequency-dependent seismic wave amplification due to topographic site effects (Harp and Jibson, 2002; Sepúlveda et al., 2005; Lee et al., 2009a, b; Khan et al., 2020). Through topographic resonance and refraction of waves, seismic amplification can reach factors of 2-14 in the horizontal component at specific frequencies, predominantly triggering landslides at mountain tops and ridge

75 crests facing away from the epicenter (Meunier et al., 2008; Bakun-Mazor et al., 2013; Rault et al., 2020; Weber et al., 2022). Moreover, seismic waves can be amplified and polarized within unstable rock mass itself due to existent open cracks, mainly perpendicular to them (Burjánek et al., 2010, 2012). Gischig et al. (2016) found through modelling that amplification factors increase and become more complex in space and frequency with a higher degree of slope damage, which may in turn be used for assessing the slope´s criticality. However, comprehensive site-specific analyses of how seismicity controls the preparation

80 phase of rock slope failures based on field observations and historical earthquakes are usually not performed.

In this study, we focus on massive rock slope failures (>20,000 m^3). As a case site we use a well-prepared high-magnitude alpine rock slope instability in dolomite rock at the summit of the Hochvogel mountain (2592 m a.s.l., see details in Section 2), where we have more than four years of multi-method high-resolution monitoring data available. Due to its magnitude, location and altitude, some generic drivers or triggers can be supposed irrelevant (Fig. 1). Strong temperature gradients and freeze-

85 thaw cycles can only affect surface-near rock mass (Bakun-Mazor et al., 2013; Weber et al., 2017) without reaching deeper-seated sliding zones. Wind and lightning strikes can potentially induce small scale rockfall, but significant influence on several thousand cubic meters of rock is unrealistic. Excluding large-scale slope engineering, this likewise holds for human or animal activity. As the Hochvogel rock slope instability is located at the summit of the mountain, no rock or ice fall can impact on the instability. The same applies to snow or rock avalanches. Volcanic activity is absent in this region. Due to its altitude, the

90 Hochvogel summit is above the treeline but below the permafrost limit. Thus, four relevant drivers remain and are therefore extensively analysed in this study: rain provided water, snowmelt derived water, rock fracturing and earthquakes. Here, we analyse displacements as the phenomenological result of all drivers and correlate them with meteorological data, local seismic recordings and earthquake catalogues. This approach allows to quantitatively evaluate promoting and triggering factors for massive rock failures similar to our case study.

95 2 Study site and instrumentation

The Hochvogel (2592 m a.s.l.) is a dominant and outstanding peak in the eastern Allgäu Alps on the border between Germany and Austria consisting of brittle, well layered dolomite rock (Hauptdolomit) with incidental marly interlayers. The summit area is characterized by a 2-6 m wide main crack that divides the massif into a stable NE-side and an unstable SW-side. The total unstable volume sums up to 260,000 m^3 above a distinct 1 m thick marly layer (Fig. 2a-A, Leinauer et al. (2020)). Including a

100 potentially unstable mass below, the total volume reaches 400,000-600,000 m^3. The rock slope instability has been developing at least since the 1940s with higher deformation rates of about 2 $\mathrm{cm\,a^{-1}}$ during the last two decades and is currently preparing to (partially) fail. Several lateral cracks at the almost vertical SW-wall have shown higher activity in the last decade. This flank shows frequent failure of rock towers, as for example a 130,000 m^3 rockfall in 2016 (Fig. 2a-B, Barbosa et al. (2023)). The site

has been under comprehensive monitoring since 2018/19 (Leinauer et al., 2021; Dietze et al., 2021), including observation of
105   crack opening, temperature, rain and seismic signals. A detailed description can be found in Leinauer et al. (2020).
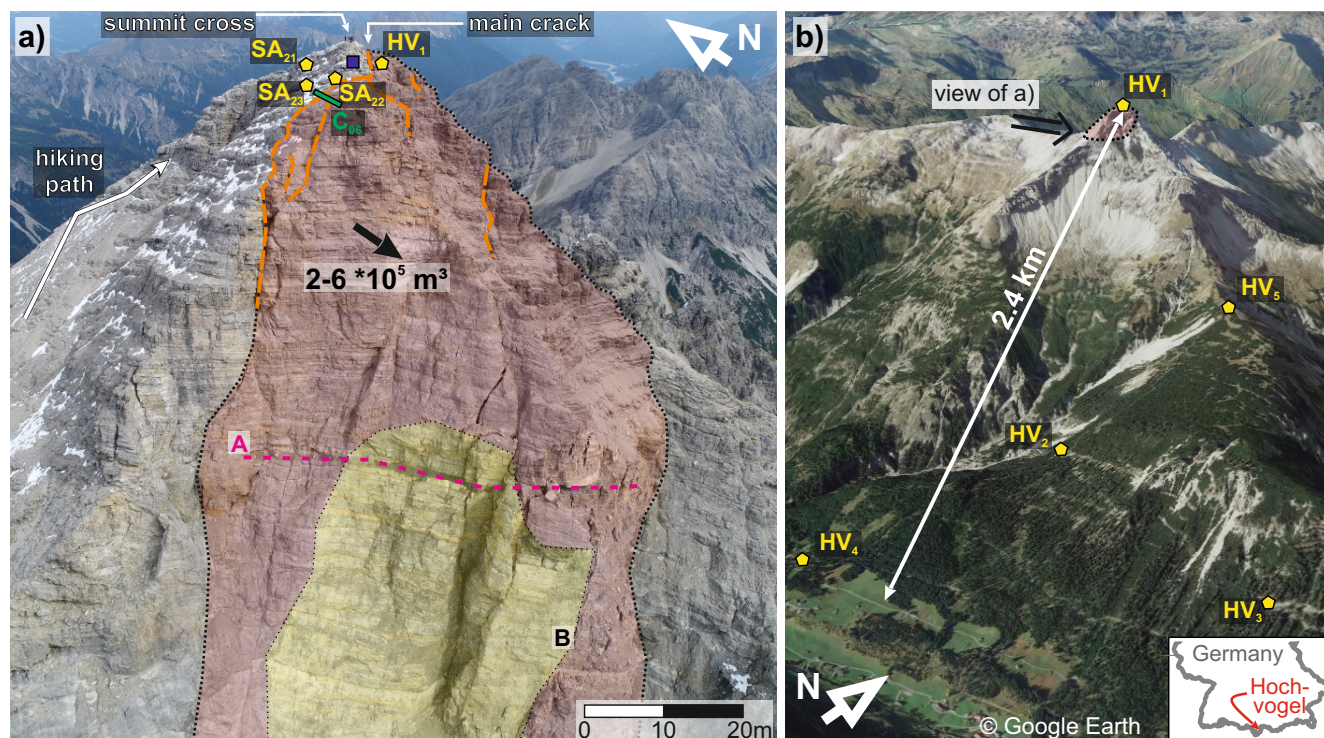

Figure 2. Overview of the study site. (a) Photo of the summit area and the steep SW-wall. The unstable mass is marked with the red area, obvious cracks are traced by dashed orange lines. Measurement devices in this study include the stations of the seismic summit network (yellow pentagrams), rain gauge (blue square) and crackmeter "C06" (green line). A distinct 1 m thick marly layer is marked by the dashed magenta line (A). The source area of a 130,000 m^3 rockfall from 2016 is marked by the yellow colour (perimeter B). (b) Hochvogel mountain with the unstable mass at the summit (red area) and the seismic stations of the flank network (yellow pentagrams). The village Hinterhornbach (AT) in the valley below the Hochvogel is in the bottom left of the image. Image source: © Google Earth.

In this study, we exploit several high-resolution data from between October 2018 and November 2022. This includes displacements measured as crack opening by a vibrating wire crackmeter (Crack06) at the most active lateral crack (see photos in Fig. S1 and S2). Measurements are available with 10 min frequency from our real-time monitoring system (resolution 0.04 mm, accuracy $\pm$ 0.15 mm). With the same frequency, the air temperature is measured directly at the crackmeter and
110   rainfall is measured with a non-heated tipping bucket rain gauge (resolution 0.1 mm, see photo in Fig. S3).

To monitor seismic processes, we installed a local seismic network on the summit consisting of 4 PE6B 4.5 Hz 3-component geophones and Digos DataCube3ext loggers (maximum distance 75 m). Three of the sensors (SA_{21}, SA_{22}, SA_{23}) are on the stable side, and one station (HV_1) is on the unstable side next to the main crack (Fig. 2a, see photos of the seismic stations in Fig. S4 and S5). Additionally, we have installed a wider network with spacings between 0.9 and 1.6 km on the SW flank below

115 the summit, consisting of TC120s or PE6B geophones and DataCube3ext or DataCube3extBOB loggers (Fig. 2b). All stations
     recorded ground velocity values at 100-400 Hz, but signals have been uniformly aggregated to 100 Hz before further analysis.
     The station meta data are listed in Table S1.

     Data for snowmelt modelling come from two stations of the Bavarian Avalanche Warning Service in the region of the
     Hochvogel (yellow diamonds in Fig. S26) that measure all necessary parameters (wind, surface and air temperature, snow
120 height). The Nebelhorn (2075-2220 m a.s.l.) station is 9 km away from the Hochvogel, the Zugspitze station (2420-2960 m a.s.l.)
     41 km.

     To analyze the effect of local or regional earthquakes, we exploit the earthquake event catalogues of Germany (BGR, 2023)
     and Switzerland (SED, 2023) containing all registered regional earthquakes with M_w >2 since 1692 and 250 AD, respectively.
     Continuous observations with sub-second resolution are available since 1975 and 2009, respectively. To study the effect of
125 strong distant earthquakes during station operation of our local seismic network, we use the catalogue of the US Geological
     Service (USGS, 2023).

3 Data processing

     All data were processed with the software R v. 4.3.0 (R Core Team, 2023). R scripts of all major processing and analysis steps
     are available in an online repository under https://doi.org/10.5281/zenodo.10567098 (Leinauer, 2024). For the availability of
130 the underlying data see the code and data availability statement.

3.1 Seismic crack events

     All seismic analysis was performed with the R package eseis v. 0.7.3 (Dietze, 2018a, b). To get corrected ground velocity time
     series (m/s), the seismic data were deconvolved according to each instrument specifications (see Table S1). Using the data
     from the summit network, we isolated discrete seismic events. We selected all times during which at least two stations operated
135 simultaneously (860 days, 60 % coverage) to include only events that were captured by more than one station. The basic picking
     routine then followed the approach by Dietze et al. (2021), using a classic short-term average/ long-term average (STA-LTA)
     ratio picker (Allen, 1882), applied to the 20–40 Hz filtered signal envelopes (on-ratio = 6, off-ratio = 1, STA-window = 0.2 s,
     LTA-window = 120 s). With these settings, even low-energy events were detected, but also many false positives. The following
     automatic check of potential events premises an event duration of 0.2-5 s as the typical duration of discrete rock fracturing
140 activity at the summit (e.g. Senfaute et al., 2009; Dietze et al., 2017a, 2021). Furthermore, the detection time difference
     between two stations needs to be less than 0.3 s according to a conservative wave travel time across the entire network. This
     excludes signals with longer detection time differences that result from the coincidence of unrelated signals or waves initiated
     by sound travelling through air. This led to a detection of 109,492 picked potential events for which we plotted seismograms
     and spectrograms. A meaningful localization of of the signal source was hindered due to the steep and complex topography,
145 strong jaggedness of the rock mass and unclear wave velocity distribution (cp. Helmstetter and Garambois, 2010).

Finally, to sort the picked events into two groups of seismic rock fracturing events (= target) and other events (steps of humans, rockfalls, coincident noise, false detections), we filtered the events further and used machine learning with a Random Forest classifier (Breiman, 2001), that has been developed in multiple processing steps. First, we calculated the signal-to-noise (SNR) ratio and re-defined all start and end times of the events with a kurtosis picker (Baillard et al., 2014; Hibert et al.,

150   2017), that can identify the picked onset more accurate than the robust STA/LTA picker used in the first step. We then rejected events without distinct ending where the picker could not identify a sharp decrease of the signal (4,813 events, usually humans walking next to the stations or signals with >5 s duration or high background noise not connected to cracking). We further rejected events where the kurtosis picker did not trigger (1,128 events), where the two picking routines identified start times differing more that 1 s (2,071 events) and events where the kurtosis-picked event ended before the start of the STA/LTA-pick

155   (12,560 events, usually when there was not one discrete isolated event). The Random Forest classifier requires a set of features that describe the seismic signal and allow to separate between the different classes. We followed and adapted the approach by Hibert et al. (2017) and calculated a set of 61 statistical values from the waveform, spectral and pseudo-spectrogram domains. We did this for the station with the highest SNR at each of the remaining 88,920 events, once for the event itself and once for a longer signal including 3 s buffer before and after the picked signal start and end times. Together with maximum SNR,

160   minumum SNR, mean duration and the duration difference between the stations per event, we used a total number 124 features as Random Forest input (see details in the Table S2).

In a first step, we created a training data set by manually classifying 1,353 events (205 crack events, 1,148 others) looking at the features in the plots described in Dietze et al. (2021). We used a balanced proportion of 80 % of the data for training and validating implementing a 5-fold cross-validation. We set up a Random Forest with 500 decision trees includ-

165   ing hyperparametertuning with random search and 1000 iterations on the minimum size of terminal nodes, the maximum number of terminal nodes and the number of variables randomly sampled as candidates at each split (see the code under https://doi.org/10.5281/zenodo.10567098 for details). In the last step we tested the performance of the classifier with the remaining 20 % unseen data. To avoid a misclassification of seismic crack events, we defined a high true-positive rate of 0.9 by setting the prediction cutoff threshold accordingly (see Fig. S7). In our case, all events were classified as crack events if

170   the probability according to the prediction model was 17.2 % or higher. This, of course, lead to a moderately higher number of false-positives (15 %). The best performance was reached using all available features. Using only selected features did not improve the classifier (see the variable importance in the Fig. S8).

Finally, we predicted the class of random 10 % (8,765) of the unclassified events using the classifier trained in the first step. We then manually corrected 1,428 false positives leading to the second larger training data set with 2,072 crack events and

175   8,037 others. Using this larger data set, we trained a refined Random Forest model following the same steps as described above leading to a smaller false-positive rate of 7 % (see Fig. S9). The accuracy of the classifier is 94 % which is comparable to previous studies and in the range of human classifiers (Provost et al., 2017; Hibert et al., 2017; Wenner et al., 2021; Langet and Silverberg, 2023). With this refined model we classified all events leading to a dataset of 21,801 seismic crack events and 67,119 others.

7

3.2   Snowmelt modelling

We modelled the amount and timing of snowmelt by simulating the dynamic evolution of the snow cover using the one-dimensional open-source software SNOWPACK (Lehning et al., 1999). With meteorological measurements as inputs, SNOW-PACK is capable of replicating snow microstructure, layering, and its interactions with the surrounding environment. The Bavarian Avalanche Warning Service provided input data, recorded at 10-minute intervals. This includes incoming and out-going shortwave radiation, snow depth, relative humidity, air temperature, total precipitation, snow surface temperature, and wind speed/direction. Simulations were conducted individually for Zugspitze and Nebelhorn and for each hydrological year from October 1 to September 31, using 15-minute time steps. The measured snow depth functioned as a proxy for precipitation inputs, influencing the mass balance. To address data gaps, the internal MeteoIO pre-processing library was employed. Where necessary, we included a constant ground temperature of 0°C and an albedo estimation from shortwave radiation.

The model parameters (see Section S3) were adjusted for each simulation to best fit the melting phase, although discrepancies between modelled and measured snow heights remained possible due to model limitations. The main output for this study was the quantity of snowmelt, expressed in $\mathrm{kg\,m^{-2}}$, which represents the amount of liquid water flowing from the snow cover into the ground. As the Hochvogel is situated between Nebelhorn and Zugsitze (in position and altitude), we used the mean snowmelt of the two sites for further analysis, except for the melting season 2021, where Nebelhorn data were not available.

3.3   Synoptical time series analysis

To correlate deformation, rainfall, snowmelt, seismic and temperature data, we aggregated all data to hourly values and created common time series plots (Fig. 4 and 3). For better comparability we used derived rates for all variables except the temperature data set (e.g., deformation rate, rainfall intensity and snowmelt in $\mathrm{mm\,h^{-1}}$, crack rate in $\mathrm{events\,h^{-1}}$ and temperature in °C). Due to the strong instrumental and diurnal noise in combination with partly very low signal rates, we smoothed all curves to uncover the measured process dynamics. We used smoothing window lengths with centered running means between 1.5 and 7 d depending on the SNR and the observed process (see captions of plots for individual values). Columns in each sub-plot represent 12 h non-smoothed means.

Based on an apparent correlation of variable pairs, we have identified three types of proxy behaviour: deformation during rain events, displacements in the snowmelt phase and thermally driven rock cracking. Within the complete time series, we identified 15 focus time periods highlighting the relationship of the particular variables. For each focus period we performed a detailed analysis (Fig. 5 to 10 and Fig. S10 to S18), including a time series plot of the two selected variables to illustrate their correlation (subplot a). Mathematically, we tested the correlation via a cross-correlation analysis of the two curves (subplot b). Here, we only considered positive time lags between the driver (e.g., rain) and the result (e.g., deformation). For the time lag with the highest correlation coefficient, we then created a scatterplot with accordingly shifted data and fitted a linear regression (subplot c).

To extend the analysis over the complete available time series, we additionally performed a running cross-correlation analysis. For two selected variables, we calculated the cross-correlation function on a subset of the data with window lengths
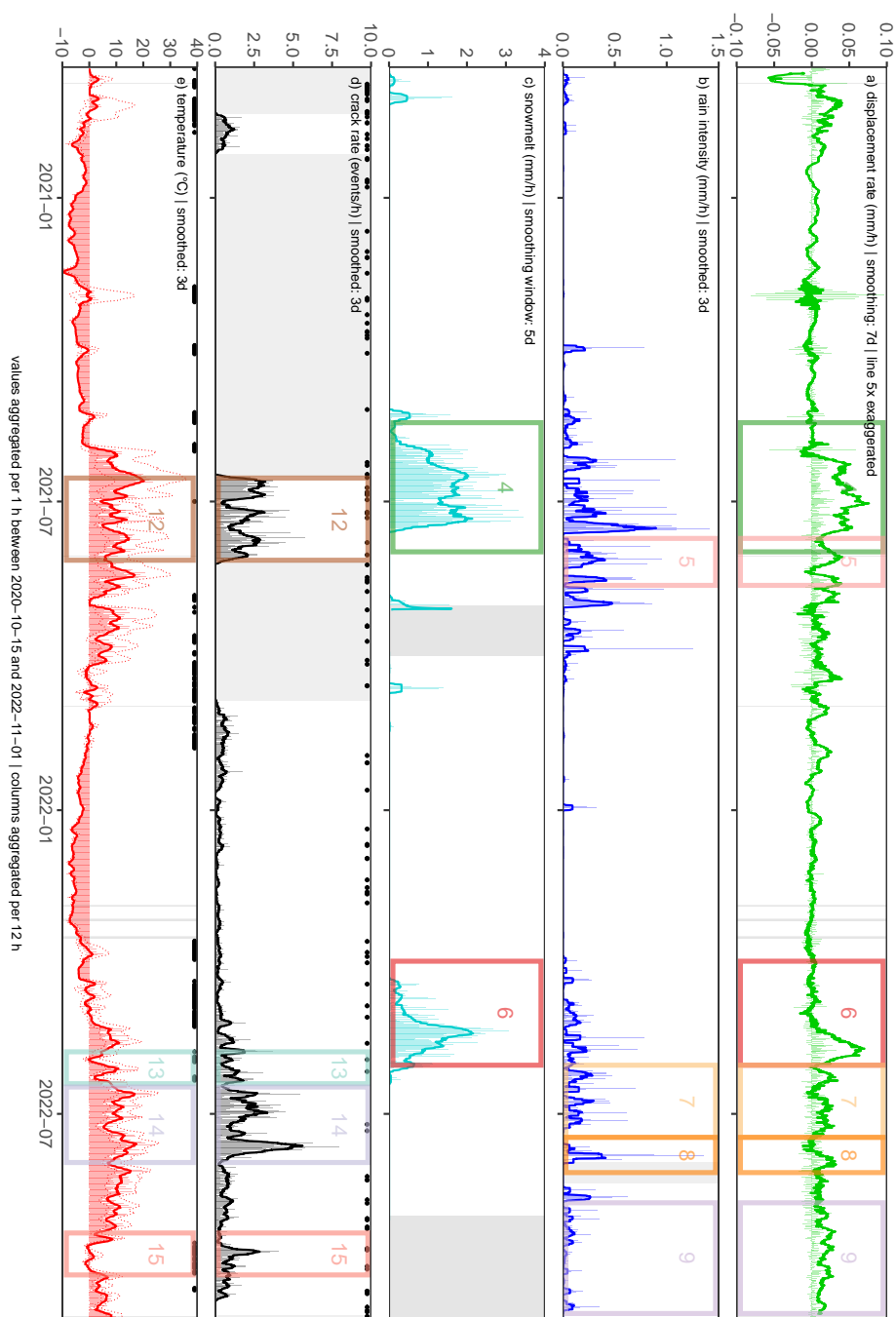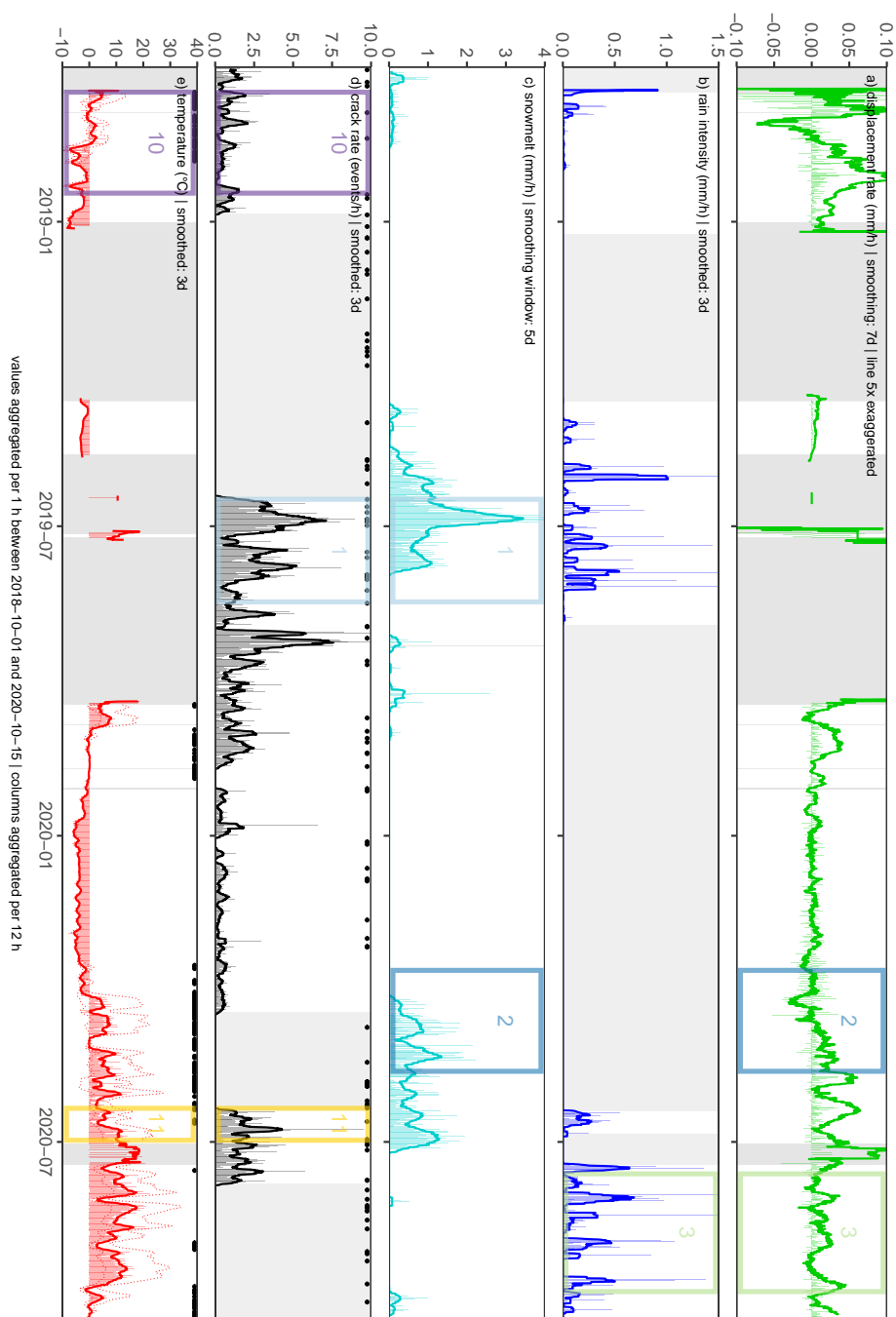
Figure 3. Analysed data between Oct 2020 and Nov 2022 with marked and numbered focus times (rectangles). Data are aggregated to 1 h resolution (see the degree of smoothing in the headers). Columns give 12 h means. (a) displacement rate (mm/h), (b) rain intensity (mm/h), (c) snowmelt (mm/h), (d) seismic crack rate (events/h), black dots mark the timing of earthquakes from the catalogue, (e) mean temperature (°C), dashed lines give min and max values, black dots mark days with freeze-thaw/ thaw-freeze conditions.

Figure 4. Analysed data between Oct 2018 and Oct 2020 with marked and numbered focus times (rectangles). Data are aggregated to 1 h resolution (see the degree of smoothing in the headers). Columns give 12 h means. (a) displacement rate (mm/h), (b) rain intensity (mm/h), (c) snowmelt (mm/h), (d) seismic crack rate (events/h), black dots mark the timing of earthquakes from the catalogue, (e) mean temperature (°C), dashed lines give min and max values, black dots mark days with freeze-thaw/ thaw-freeze conditions.

between 20 and 60 d depending on the observed process. We iterated this by moving the analysis window in 1 d steps and plotted the correlation coefficient for several time lags against the time (Fig. S19 to S25).

215 ### 3.4 Newmark displacement and topographic amplification

We calculated the theoretical Newmark displacement using a well-introduced regression model with the formula after Jibson (2007, Eq. 9):

$$log \; D_N = 2.401 \; log \; I_a - 3.481 \; log \; a_c - 3.230 \pm 0.656 \qquad (1)$$

where D_N is the Newmark displacement in cm, I_a is the Arias Intensity in $\mathrm{m\,s^{-1}}$ and a_c is the critical acceleration in terms

220 of g (the gravity constant). The critical acceleration a_c in $\mathrm{m\,s^{-2}}$ depends on the factor of safety (FOS, ratio of resisting forces over driving forces) of the area of interest and the sliding plane's slope angle α in degrees (Newmark, 1965; Jibson, 1993):

$$a_c = (FOS - 1) \; sin \; \alpha \qquad (2)$$

The Arias Intensity can be estimated after the formula (Wilson and Keefer, 1985; Jibson, 1993):

$$log \; I_a = M - 2 \; log \sqrt[2]{D^2 + h^2} - 4.1 \qquad (3)$$

225 where M is the earthquake magnitude, D is the epicenter distance in km and h is the focal depth in km.

The exact FOS at the Hochvogel instability can currently not be determined due to uncertainties in the location and condition of the sliding surface. Due to the ongoing mass movement over many decades (Leinauer et al., 2020), we assume only few remaining rock bridges in the carbonate mass and infer a FOS close to failure about 1.1 (Knapp et al., 2018; Heckmann et al., 2012). We further evaluated a variety of FOS values where a FOS of 1.05 represents conditions closer to failure, 1.2 less

230 sensitive conditions and 1.01 a slope instability that is imminently failing. We calculated all theoretical Newmark displacements for the set of FOS between 1.01 and 1.2, slope angles between 25° and 85°, magnitudes up to $M_w = 8$, distances up to D = 150 km and a focal depth of h = 8 km (mean depth in the earthquake catalogue). We assume a conservative critical Newmark displacement of 2 cm above which rockslides can be triggered (Miles and Keefer, 2001; Meyenfeld, 2009). In a magnitude-distance plot, this critical displacement appears as line per FOS (for a fixed slope angle, Fig. 11 and Fig. S28

235 to S34). To asses the possible effect of typical earthquakes in the Hochvogel region, we filtered the BGR and SED catalogues for all events with epicenter distances of less than 150 km from the Hochvogel and plotted these into the magnitude-distance plot. More distant events are considered to have no major effect. The ten events with the biggest Newmark displacements have been assessed further including the uncertainty contained in formula (1) using their exact focal depth (Fig. S35 to S41).

To assess the effect of topographic amplification we use the peak ground velocity (PGV) measured by our seismometers after

240 several earthquake events (see example record in Fig. S42). It is often complex to distinguish between topographic resonance effects and interacting localized site effects (Rault et al., 2020; Weber et al., 2022) but landslide appearance and rockfall volume correlate with high peak ground accelerations (Meunier et al., 2007; Massey et al., 2022). During earthquakes, the stability of slopes relies on the magnitude of ground motion and its frequency content (e.g. Jibson et al., 2000; Rault et al., 2020). We

therefore look at PGV values as the phenomenologial result of seismic stimulation measured by our sensors. We compare the

245 measured PGV during earthquakes at the summit station HV_1 with the stations HV_2, HV_3 and HV_5 at the flank lower in the valley and the station SA_{23} on the stable side of the summit. The station HV_4 had to be excluded due to the insufficient number of recorded earthquakes. We used all earthquake events from the BGR and SED catalogues that have been recorded on all three components (Z, N, E) of each particular station (Fig. S27). For comparison of regional and distant earthquakes, we additionally used 18 events with a distance D > 15,000 km and magnitude $M_w > 6$ from the USGS catalogue. We then

250 detected the PGV in the signal envelope in 1 Hz windows moved in 0.25 Hz steps between 0.5 and 10 Hz for all components, stations and earthquake events. The ratio of the PGV at station HV_1 against the other stations (site-to-reference ratio) is used as indicator of amplifying effects.

4   Results and discussion

4.1   Rainfall induced displacement

255 During the warm summer months after snowmelt (May or June to October) the rock mass shows accelerated movement in connection with strong precipitation events. During this period, 38 % of the total crack opening happens during wet days although these only account for 26 % of the total time. The average displacement rate is 1.8 times higher during wet periods compared to periods without precipitation. Looking at peak velocities, this effect reaches a factor of 4-5.

The direct comparison of rainfall intensity and displacement rates during the selected focus times reveals a high correlation

260 with a time lag of 1-16 h (Fig. 5 and 6, and Fig. S10 and S12). Without superposition with other effects like snowmelt, this behaviour can be observed in more than 20 rainfall events across the four summers. The lag likely accounts for the rainfall infiltration time and until maximum hydrostatic pressure is built in the discontinuities within the rock mass. Both depend on pre-event saturation as we cannot observe a consistent change in lag time throughout each season. In addition, the saturation of the discontinuity with water might eliminate the joint cohesion in some discontinuities, lower the joint friction angle especially

265 in the basal marl layers and reduce the effective normal stress at the sliding surface due to buoyancy (Erismann and Abele, 2001), leading to increased displacement rates.

We cannot identify an activation threshold, meaning that even small rainfalls can accelerate the mass movement (see focus time 9, Fig. S12). Within dry periods, timely well-constrained intense rainfall events with several $\mathrm{mm\,h^{-1}}$ accelerate the mass up to 1 $\mathrm{mm\,d^{-1}}$ (cp. August 16 in Fig. 5). When the water input decreases at the end of the rain event the unstable mass

270 decelerates. There is no permanent sealing of discontinuities and perched water drains within several hours. On the other hand, rain events that happen close together within few days result in a common velocity peak due to the retention of water in the system (cp. focus time 8 in Fig. S11). This proposes an immediate lowering of water saturation at least in the fractures in case of dry conditions but also that a proportion of the infiltrated water stays in the system for several days. This can precondition the system in case of further water infiltration, as partially to fully saturated conditions promote the build-up of hydrostatic

275 pressure. Similar observations are reported by Helmstetter and Garambois (2010), who found no minimum rain threshold for rockfall triggering, time lags of up to 1 h for rockfalls and a few days for displacement rates at the Séchilienne rockslide in the
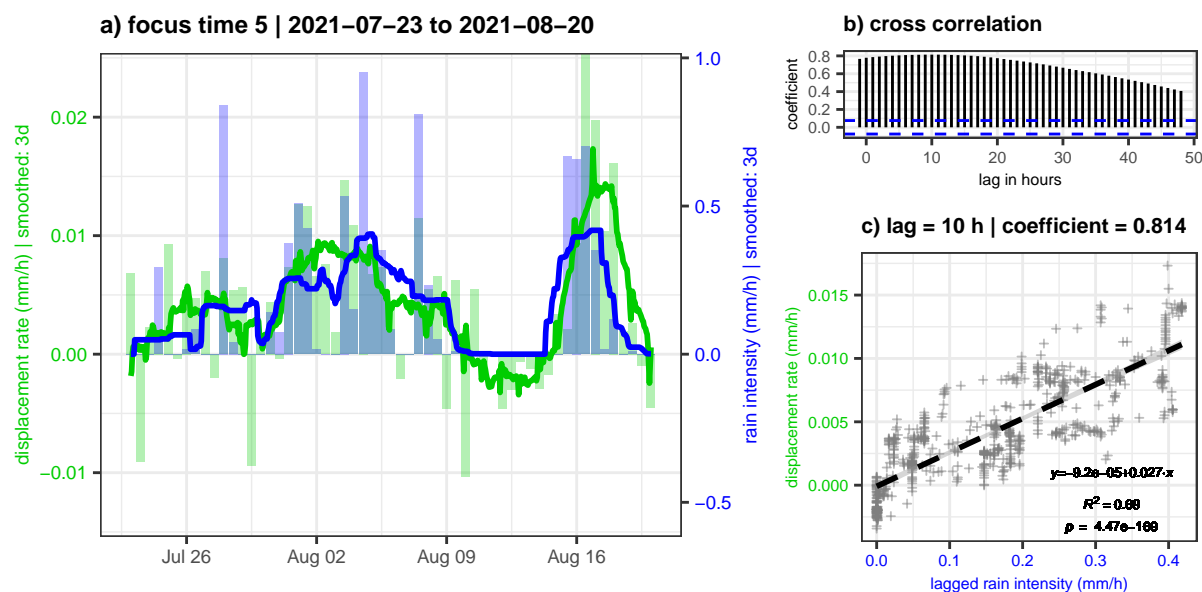
Figure 5. Detail plot of focus time 5. (a) displacement rate and rain intensity (lines 3 d smoothed, columns 12 h means). (b) cross-correlation coefficient of the two lines. The highest correlation appears with a lag of 10 h and a coefficient of 0.814. (c) scatter plot with linear trendline with 10 h shifted data.

French Alps. However, there, accelerated movements last for about a month which might be connected to the bigger size and deeper-seated sliding zone compared to the Hochvogel (50-100 million m^3 vs. 200-400 thousand m^3).

At the Hochvogel, we infer from the linear regression between rain and displacement that in general rain intensities of 0.3-0.6 $\mathrm{mm\,h^{-1}}$ trigger displacement rates of ca. 0.01 $\mathrm{mm\,h^{-1}}$. The running cross-correlation (Suppelementary Fig. 20) gives high correlation coefficients of >0.75 with small lag times each summer after snowmelt. This supports the interpretation of a rainfall controlled regime during the snow-free summers. However, the correlation coefficient fluctuates due to the short duration of rain events. The generally strong and immediate response of the rock slope to rain events is indicative of existing substantial damage and a high criticality of the slope (Gischig et al., 2016).

4.2 Snowmelt induced displacement

Snowmelt usually occurs between April and July and contributes significant amounts of water to the system, causing accelerated slope movements (Fig. 7 and 8, and Fig. S14). While melt water generally affects slope dynamics the same way as described above, our cross-correlation analysis suggests longer lag times, between 4 and 9 days. This is likely related to the slower but therefore more continuous supply of water into the rock mass. Moreover, as there is no snow station directly at Hochvogel, the snowmelt amount is modelled based on measurement data from neighbouring peaks, Nebelhorn and Zugspitze. Given that
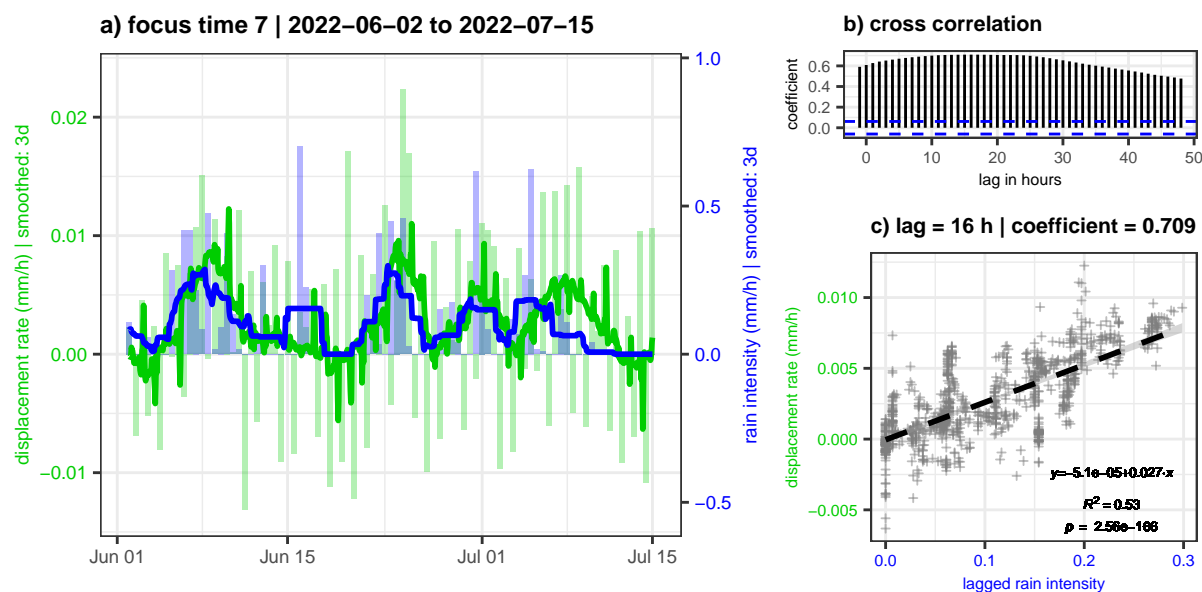
Figure 6. Detail plot of focus time 7. (a) displacement rate and rain intensity (lines 3 d smoothed, columns 12 h means). (b) cross-correlation coefficient of the two lines. The highest correlation appears with a lag of 16 h and a coefficient of 0.709. (c) scatter plot with linear trendline with 16 h shifted data.

the south-oriented slopes of the outstanding Hochvogel peak become snow-free quite early, while significant amounts of snow remain in the >10 m deep main fracture much longer, we anticipate differences in the snowmelt characteristics.

The intensity of the modelled snowmelt generally surpasses the measured rain from the summit, potentially not reflecting the accurate volume of snowmelt infiltrating into the discontinuities at Hochvogel. However, our analysis indicates that, on average,

295 modelled snowmelt of about $1.5~\mathrm{mm\,h^{-1}}$ corresponds to displacement rates of ca. $0.01~\mathrm{mm\,h^{-1}}$. Secondary peaks with higher snowmelt rates inducing temporary accelerations are visible in the velocity curve too (e.g., July 2-15 in Fig. 7 and May 20 in Fig. 8). During early summer, intense rainfall from the first thunderstorm cells superimpose with the late snowmelting phase, making it challenging to distinguish the driving processes effectively during this period. However, rain falling on snow can result in higher water infiltration than from the rainfall alone (Stock et al., 2013).

300 The running cross-correlation (Suppelementary Fig. 21) gives correlation coefficients above 0.75 with lag times of 4-9 d each year during snowmelt. This supports our interpretation of a meltwater-controlled regime during the snowmelt season. The snowmelt correlation coefficient fluctuates less than with the rain data, as the snowmelt appears more continuous than the distinct short rain events.
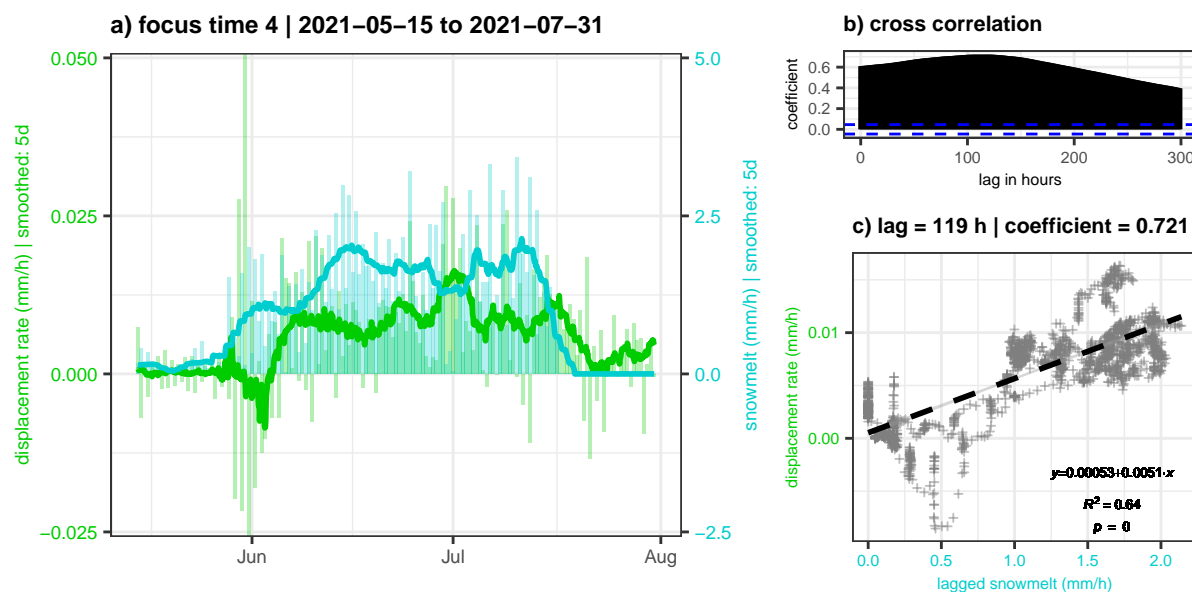
Figure 7. Detail plot of focus time 4. (a) displacement rate and snowmelt (lines 5 d smoothed, columns 12 h means). (b) cross-correlation coefficient of the two lines. The highest correlation appears with a lag of 5 d and a coefficient of 0.721. (c) scatter plot with linear trendline with 119 h shifted data.

4.3 Seismic crack events

The summit network recorded 21,801 discrete events that fall into the class of rock cracking. Their duration was $1.4^{+0.5}_{-0.4}$ s (median and quartile range), preferentially occurring during daytime, matching the conclusions of Dietze et al. (2021). On annual scale, the crack rate is higher during the summer months coinciding with higher displacement rates, higher rain fall intensities and higher temperatures (Fig. S6). We therefore analysed if rock cracking rates and displacement rates interact directly, or if the correlation is rather indirect meaning that environmental forcing increases both, crack rates and slope movement.

We could not find specific time periods where the smoothed crack rate correlates well with the smoothed displacement rate (Fig. 3 and 4). Likewise, the running cross-correlation analysis (Fig. S19) did not reveal stable high correlation coefficients with a specific time lag. This implicates that there is no obvious correlation between crack rate and displacement rate.

The same applies for the correlation between crack rate and rain fall intensity (Fig. S23). In the melting period 2019 (focus time 1, Fig. S13), we found a high correlation between 7 d-smoothed snowmelt and crack rate at a time lag of 40 h. However, this relation did not emerge in other years and it remains unclear if strong snowmelt can induce enhanced rock cracking.

In contrast, we found the crack rate peaking during temperature peaks (c.p. Fig. 9 and Fig. S15 and S16), likely related to thermal forcing through volumetric expansion and contraction of the rock mass and its minerals. Even small oscillations are represented in both curves. The maximum correlation coefficient appears with a time lag of 0-15 h. Additionally, we observed peaks of rock cracking activity during days with freeze-thaw and/or thaw-freeze conditions (Fig. 10 and Fig. S17 and S18).
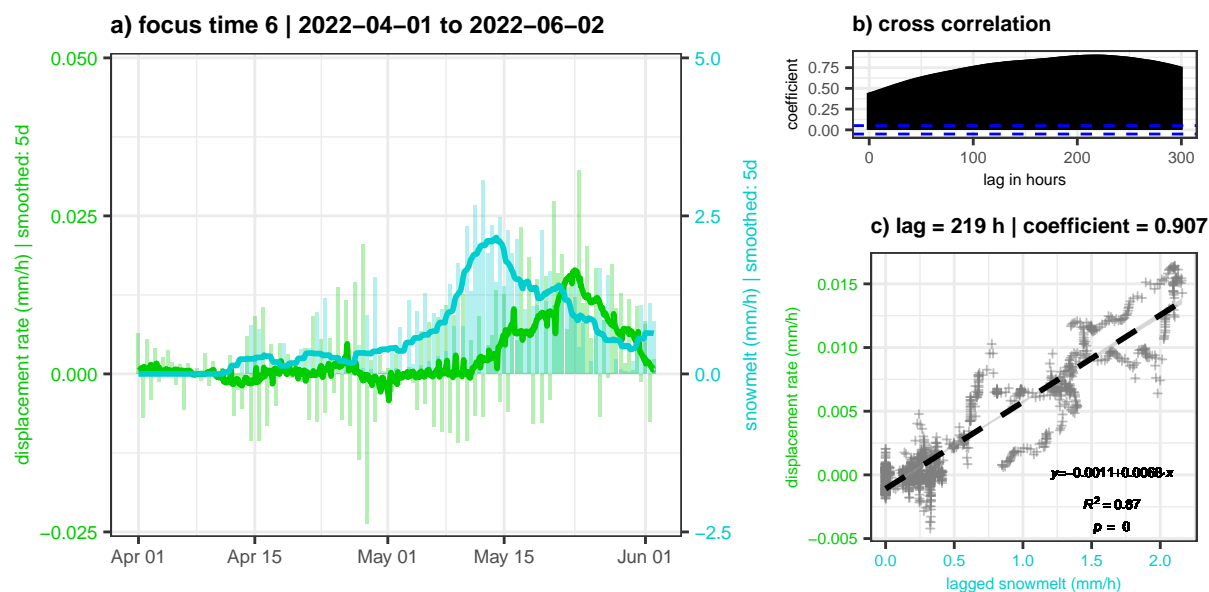
15

Figure 8. Detail plot of focus time 6. (a) displacement rate and snowmelt (lines 5 d smoothed, columns 12 h means). (b) cross-correlation coefficient of the two lines. The highest correlation appears with a lag of 9 d and a coefficient of 0.907. (c) scatter plot with linear trendline with 219 h shifted data.

320 Furthermore, the first deep frost of the season without thawing conditions seems to enhance the crack event rate for 4-5 d (e.g., November 16 and December 11 in 2018, Fig. S17). Here, stress is caused by cryogenic processes in ice-filled fractures or pores, volumetric expansion/ contraction and/or ice segregation (Weber et al., 2017).

Heat conduction in rock is relatively slow in the range of $1 \, \mathrm{cm \, h^{-1}}$ (Weber et al., 2017; Mulas et al., 2020). The fast reaction of rock cracking activity towards air temperature changes in turn means that most of the crack events that we detected
325 happened close to the surface. This is in line with the results of Dietze et al. (2021). The thermally induced stress can only affect surface-near rock mass (Bakun-Mazor et al., 2013) unless advective heat transport by percolating water or air can act in fractures (Blikra and Christiansen, 2014; Weber et al., 2017). The shallowness of the detected fracturing events can explain why there is no obvious correlation between crack and displacement rates. Displacements can only result from cracking if rock bridges fail at the sliding plane which we expect to be >10 m away from the rock surface. We assume, that we also detected
330 rock fracturing originating from the sliding plane but the frequency of those events is obscured by the dominant surface-near crack events. Lagarde et al. (2023) state that crack signals might not always be intense enough to distinguish them from other ambient seismic noise. However, this likely changes when the instability develops closer to failure and the rock fracturing frequency and intensity at the active sliding surface increases. More pronounced rock deformation in the final stage of failure will concurrently intensify the shallow cracking activity. As this activity is then less dependent on temperature changes, it might
335 still be possible to detect a precursory change in activity. On the other hand, crack rates could be altered imminently before
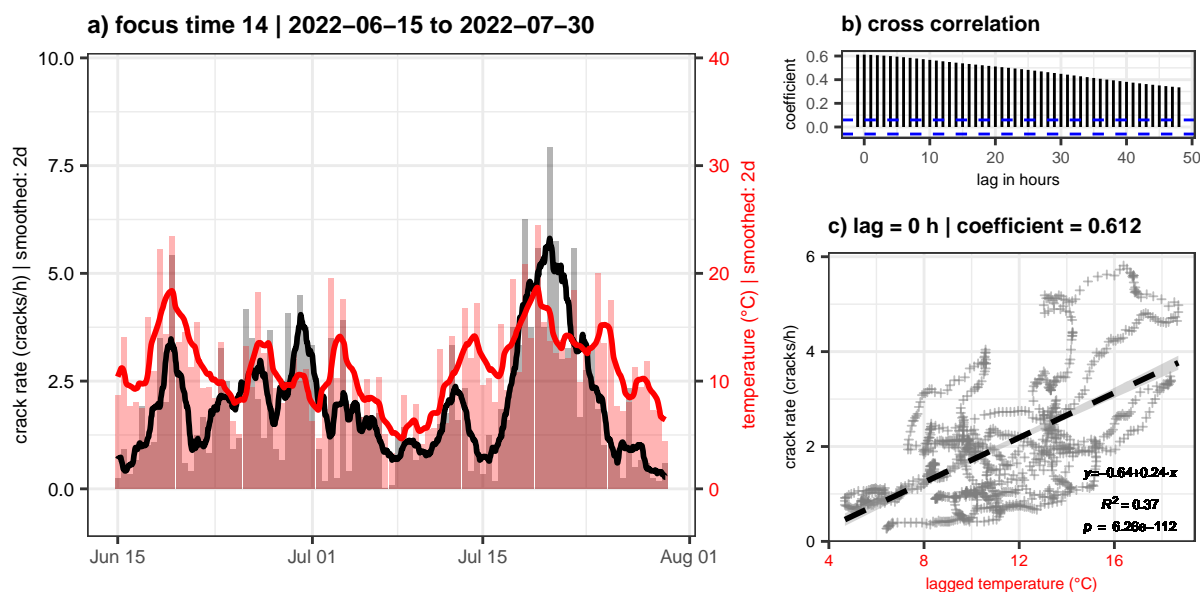
Figure 9. Detail plot of focus time 14. (a) crack rate and mean temperature (lines 2 d smoothed, columns 12 h means). (b) cross-correlation coefficient of the two lines. The highest correlation appears without any lag and a coefficient of 0.612. (c) scatter plot with linear trendline with data not shifted (0 h).

failure, when no rock bridges are left (Lagarde et al., 2023), yet it remains unclear if this can be observed at a multi-block rockslide with the size of the Hochvogel.

4.4 The effect of earthquakes and topographic amplification

The analysis of the earthquake catalogue yielded coincidence of a major earthquake with a major rockfall at the Hochvogel in one case only, on June 30, 1935, three days after a M 5.2 earthquake in Bad Saulgau in a distance of 103 km (Hutter, 2010). Potentially, several historical rockfalls at the Hochvogel might not be documented. An event-specific analysis is therefore not productive and thus we included the whole available earthquake database into our analysis (Fig. S26). It shows that a low-energy background activity is present, mainly originating in the tectonically active alpine valleys, but close high-magnitude events are rare (only 2 events $> M_w$ 5.5 since 1900). This frequent seismic activity could contribute to a low-level promotion of slope instabilities through seismic fatigue. Gischig et al. (2016) could show that earthquake-induced displacements can vary by more than two orders of magnitude depending on pre-existing damage. However, they used a model with several events with magnitudes $> M_w$ 5.7 and shorter distance. For the Hochvogel, a direct comparison of earthquake timings (black dots in Fig. 4d and 3d) with crack or deformation rates did not show obvious significant influence.

To evaluate the potential of earthquakes in the Hochvogel region to immediately trigger a major rockfall event, we conducted the Newmark analysis. The calculation of all theoretical Newmark displacements in the magnitude-distance plot (Fig. 11) illus-
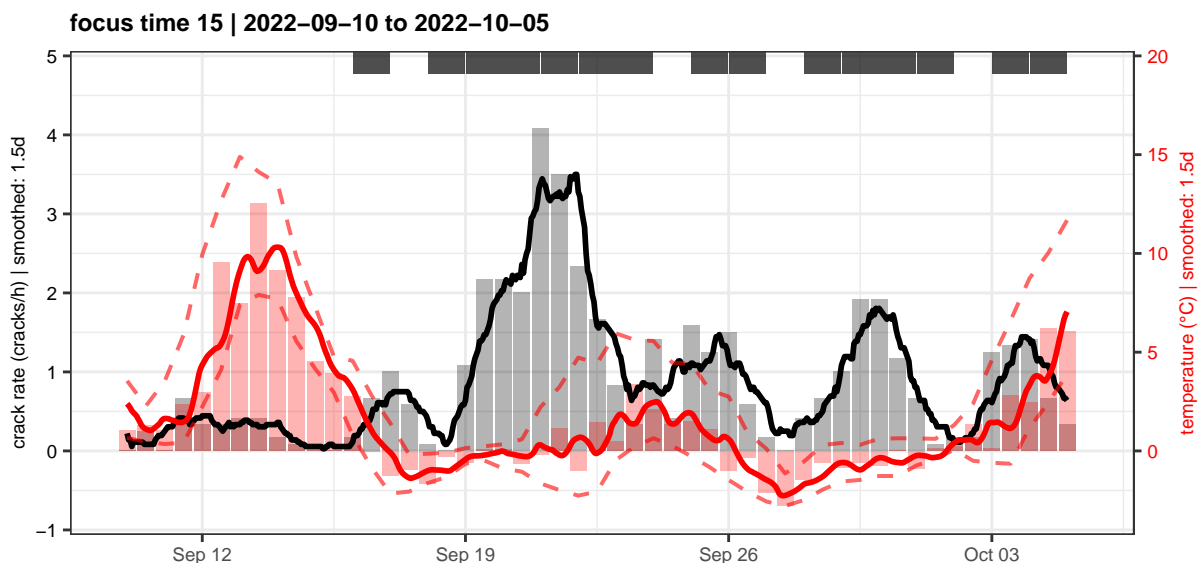
17

Figure 10. Detail plot of focus time 15. Crack rate, mean temperature (solid line), minimum and maximum temperature (dashed lines, all lines 1.5 d smoothed, columns 12 h means). Peaks in the crack rate coincide with days with freeze-thaw or thaw-freeze conditions (black bars on top). The cross-correlation is not shown due to the missing correlation of both curves.

trates how strong an earthquake must be at what distance to have the potential to trigger a rockslide. From the >5,000 historical earthquakes in the database, only very few events are in the range of having triggering potential for very low FOS <1.03. A further analysis of the ten events from the catalogue with the biggest Newmark displacements including the uncertainty contained in formula (1) confirms this implication (Fig. S35 to S41). Thus, typical earthquakes around the Hochvogel (e.g. M_w 5

355   in 20 km distance or M_w 6 in 100 km distance) might only be able to trigger a major rockfall, if the unstable mass is anyways very close to failure (FOS around 1.01). As we interpret the current FOS to be between 1.05 and 1.1, only an exceptionally strong earthquake (e.g. M_w 6 in 15 km distance or M_w 7 in 50 km distance) could immediately trigger a major failure. Recurrence intervals for such events in this area are estimated to vary between 1,000 and 2,000 years (Oswald et al., 2022). The previously identified 1935 Bad Saulgau event was too weak to have a clear triggering potential. The biggest, but still very

360   moderate displacement is indicated by the historic 1930 Namlos earthquake (M_w 5.3-5.5, 20 km distance). This event induced enhanced mass wasting processes recorded in local lakes (Oswald et al., 2022), but did not trigger any high-magnitude slope failures (Oswald et al., 2021).

    The evaluation of low earthquake triggering potential holds, although we used a conservative threshold for the critical Newmark displacement of 2 cm. Other studies suggested even higher thresholds between 2-15 cm (Wilson and Keefer, 1985;

365   Jibson et al., 2000; Miles and Keefer, 2001; Meyenfeld, 2009). Additionally, we checked the regression estimate of the Arias intensity with earthquake signals that could be recorded with our local stations. In theses cases, the formula (3) after Wilson and Keefer (1985) overestimates the Arias intensity about 1-2 magnitudes compared to the direct determination after Arias
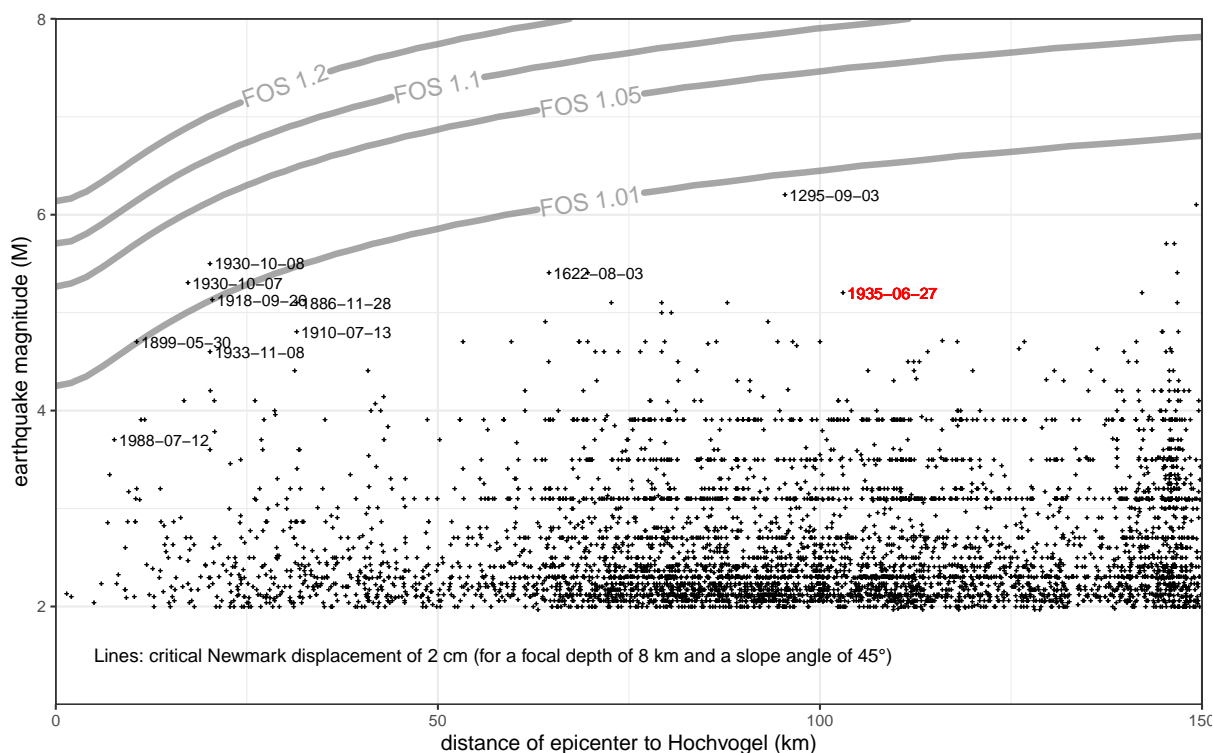
18

Figure 11. Lines indicate for different factors of safety, at which magnitude and distance of an earthquake a theoretical Newmark displacement of 2 cm is expected. This calculation is based on the mean focal depth of 8 km and the mean slope angle of the Hochvogel SW flank (45°). All earthquakes from the catalogues are plotted with black crosses. The earthquakes with the 10 biggest Newmark displacements are labelled in black with their dates. The Bad Saulgau 1935 event is labelled in red. Plots for all other slope angles are in the Supplementary Material.

(1970) with the measured ground motion values from our stations. But still, the calculated Newmark displacements are below the threshold.

370   However, this evaluation could change under the influence of topographic amplification. The geomorphological shape of the Hochvogel massif as well as the location of the unstable mass at the ridge generally favour the effect of topographic amplification (Meunier et al., 2008; Lee et al., 2009a; Khan et al., 2020; Rault et al., 2020). A comparison of the measured peak ground velocity (PGV) during earthquakes at the summit station HV_1 against the lower stations shows up to 11 times higher median PGVs at the summit (mean = 3.2, Fig. 12). The extent of this effect varies between the horizontal (E_{mean} = 4.5,

375   N_{mean} = 3.4) and vertical components (Z_{mean} = 1.7), which is typical for topographic amplification (e.g. Bakun-Mazor et al., 2013; Burjánek et al., 2012; Weber et al., 2022), but it remains consistent across the various stations at the valley flank. The horizontal components show the first low-frequency amplification factor peak between 1.5-3 Hz, which is probably around the fundamental resonance frequency of the Hochvogel mountain. Weber et al. (2022) determined a fundamental frequency of

1.8 Hz for the Grosser Mythen, a mountain of comparable shape and similar scale. The amplification effect at the Hochvogel is least pronounced when referencing to the highest valley station HV_5 (1933 m) that is situated on a ridge (mean of E-component medians: $HV_2 = 4.5$, $HV_3 = 4.2$, $HV_5 = 3.8$). This is in line with the results of Weber et al. (2022) who measured a mean amplification factor of 9 at the Matterhorn summit and 5 at a ridge below. In general, there is no major difference in median PGV ratios between the local and the far earthquakes. A directional analysis of earthquake epicenters is yet not meaningful due to the limited number of recorded earthquakes.

This could indicate that the summit experiences a significant amplification of factor 2-11 due to topographic site effects and resonant amplification. Then, true displacements due to earthquakes are higher than predicted by the theoretical Newmark displacement analysis and thus the triggering potential is higher than previously assumed. Likewise, the importance of seismic fatigue as a promoting driver is increased by topographic amplification. However, PGV ratios are >1 at station SA_{23} too, which is very close to HV_1 but on the stable side of the summit. The general theory would expect a similar amplification at the two summit stations and thus a ratio close to 1. In the low frequencies <4 Hz, there is no amplification peak at station SA_{23}, other than at the other stations further down the valley flank. This could be a result of similar site effects at the two summit stations, but still, higher PGVs have been recorded at the HV_1 station. This might be due to an amplification and polarization within unstable rock mass itself due to the open main and lateral cracks (Gischig et al., 2016). Burjánek et al. (2010, 2012) measured similar amplification factors with strong variations on the slope scale on two slope instabilities. It is possible that the unstable mass of the rock slope instability close to the wide open and deep main fracture reacts stronger to ground motions than the intact bedrock on the stable side of the summit. As we set up all stations the same way, we assume that all stations have a comparable coupling to the ground. Hence, any differences are supposed to be due to different material properties below the stations, e.g. a massive rock block at the summit and a weathered layer further down the flank. However, large amplification factors and a strong spatial heterogeneity across the rock slope may indicate a high criticality of the slope (Gischig et al., 2016). If the seismic amplification and its heterogeneity increases in future monitoring, it could be used as a precursory sign for imminent failure.

5 Conclusions

We processed more than four years of high-resolution monitoring data from a very active alpine rock slope instability including displacement, rain, snowmelt, temperature and seismsic observations to quantify the main drivers and their triggering potential. This methodological procedure can be transferred to similar cases. At the Hochvogel, the acceleration of the unstable mass even due to small environmental impacts proves a highly sensitive close-to-failure status, at least for parts of the summit.

1. During the *snowmelt phase in spring*, displacements are controlled by meltwater infiltration. The cross-correlation analysis indicates a time lag of 4-9 days between snowmelt input and landslide velocity.

2. During the *snow-free summer*, rainfall controls displacement rates with a time lag of 1-16 h, indicating the possibility of fast hydrostatic pressure increase in the system. Even small rainfalls can accelerate the mass and previous water
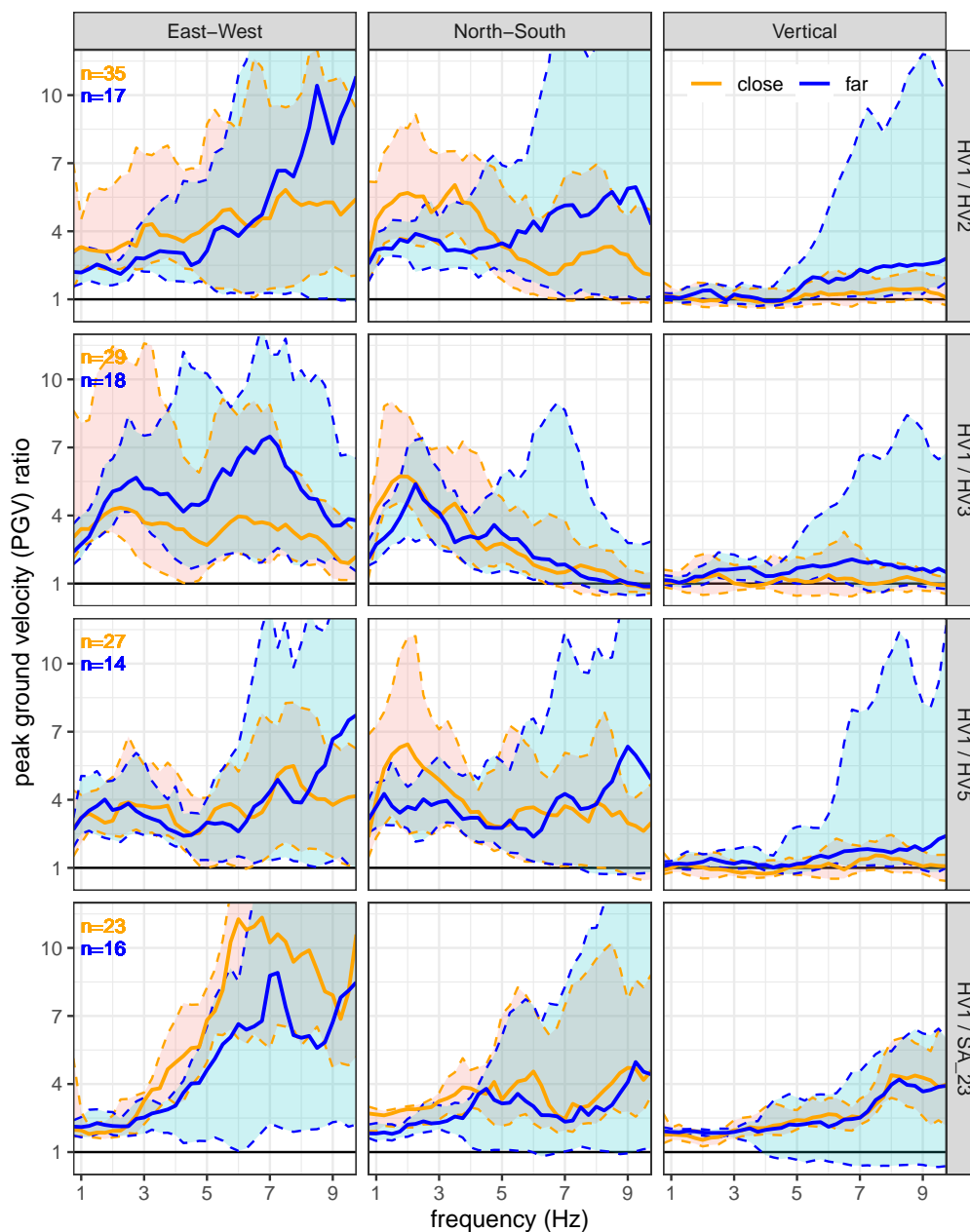
Figure 12. Ratio of measured peak ground velocity (PGV) of HV_1 on the unstable side at the summit against other stations for close (<150 km, orange) and far (>15,000 km and M>6, blue) earthquakes. The solid line marks the median and the dashed lines the 10th and 90th percentiles. HV_2, HV_3 and HV_5 are located further down the flank, SA_{23} is located on the stable side of the summit.

infiltration preconditions the system in case of consecutive rain events for few days. The rock cracking frequency is mainly controlled by high temperature with a time lag of 0-15 h indicating that we mostly detected surface-near crack events.

3. During the *first frost of the season in autumn*, days with freeze-thaw cycles or clear negative temperatures show higher crack rates. The crack rate might secondarily be controlled by snowmelt or rainfall with low correlation, but it seems not to correlate with displacement directly.

4. During *frozen conditions in winter*, the landslide activity is generally low.

According to our Newmark analysis, recent and historic earthquakes are too weak to have an immediate triggering potential for a major failure at the Hochvogel, unless the FOS is already very close to 1. Seismic topographic amplification of the peak ground velocity of factor 2-11 in the low frequencies is likely and the spatial and frequency-wise heterogeneity of amplification at the summit suggests a high damage and criticality of the slope. In summary, we identified water from rain and snowmelt to be the main driving factor. Future increases of rock mass displacements following small environmental impacts as well as changes in the seismic response to earthquakes can express a development towards higher criticality. In the light of ongoing climatic changes that lead to more frequent and intense heavy precipitation events and faster snowmelt, our findings suggest that the Hochvogel and similar unstable alpine rock slopes may experience stronger environmental forcing in the future.

References

Allen, R.: Automatic phase pickers: Their present use and future prospects, Bulletin of the Seismological Society of America, 72, 225–242, 1882.

Amitrano, D. and Helmstetter, A.: Brittle creep, damage, and time to failure in rocks, Journal of Geophysical Research, 111, https://doi.org/10.1029/2005JB004252, 2006.

Arias, A.: A Measure of Earthquake Intensity, in: Seismic Design for Nuclear Power Plants, edited by Hansen, R. J., pp. 438–483, Massachusetts Inst. of Tech. Press, Cambridge, Mass., 1970.

Baillard, C., Crawford, W. C., Ballu, V., Hibert, C., and Mangeney, A.: An Automatic Kurtosis-Based P- and S-Phase Picker Designed for Local Seismic Networks, Bulletin of the Seismological Society of America, 104, 394–409, https://doi.org/10.1785/0120120347, 2014.

Bakun-Mazor, D., Hatzor, Y. H., Glaser, S. D., and Carlos Santamarina, J.: Thermally vs. seismically induced block displacements in Masada rock slopes, International Journal of Rock Mechanics and Mining Sciences, 61, 196–211, https://doi.org/10.1016/j.ijrmms.2013.03.005, 2013.

Ballantyne, C. K., Sandeman, G. F., Stone, J. O., and Wilson, P.: Rock-slope failure following Late Pleistocene deglaciation on tectonically stable mountainous terrain, Quaternary Science Reviews, 86, 144–157, https://doi.org/10.1016/j.quascirev.2013.12.021, 2014.

Barbosa, N., Leinauer, J., Jubanski, J., Dietze, M., Münzer, U., Siegert, F., and Krautblatter, M.: Massive sediment pulses triggered by a multi-stage alpine cliff fall (Hochvogel, DE/AT): [preprint] - in review, Earth Surf. Dynam. Discuss., https://doi.org/10.5194/esurf-2023-10, 2023.

BGR: Deutscher Erdbebenkatalog: Bundesanstalt für Geowissenschaften und Rohstoffe, https://services.bgr.de/geophysik/gerseis, 2023.

Blikra, L. H. and Christiansen, H. H.: A field-based model of permafrost-controlled rockslide deformation in northern Norway, Geomorphology, 208, 34–49, https://doi.org/10.1016/j.geomorph.2013.11.014, 2014.

Borri-Brunetto, M., Carpinteri, A., and Chiaia, B.: The Effect of Scale and Criticality in Rock Slope Stability, Rock Mechanics and Rock Engineering, 37, 117–126, https://doi.org/10.1007/s00603-003-0004-1, 2004.

Breiman, L.: Random Forests, Machine Learning, 45, 5–32, https://doi.org/10.1023/A:1010933404324, 2001.

Burjánek, J., Gassner-Stamm, G., Poggi, V., Moore, J. R., and Fäh, D.: Ambient vibration analysis of an unstable mountain slope, Geophysical Journal International, 180, 820–828, https://doi.org/10.1111/j.1365-246X.2009.04451.x, 2010.

Burjánek, J., Moore, J. R., Yugsi Molina, F. X., and Fäh, D.: Instrumental evidence of normal mode rock slope vibration, Geophysical Journal International, 188, 559–569, https://doi.org/10.1111/j.1365-246X.2011.05272.x, 2012.

Chae, B.-G., Park, H.-J., Catani, F., Simoni, A., and Berti, M.: Landslide prediction, monitoring and early warning: a concise review of state-of-the-art, Geosciences Journal, 21, 1033–1070, https://doi.org/10.1007/s12303-017-0034-4, 2017.

Dietze, M.: The R package "eseis" – a software toolbox for environmental seismology, Earth Surface Dynamics, 6, 669–686, https://doi.org/10.5194/esurf-6-669-2018, 2018a.

Dietze, M.: 'eseis' - a comprehensive R software toolbox for environmental seismology, https://doi.org/10.5880/GFZ.5.1.2018.001, 2018b.

Dietze, M., Mohadjer, S., Turowski, J. M., Ehlers, T. A., and Hovius, N.: Seismic monitoring of small alpine rockfalls – validity, precision and limitations, Earth Surface Dynamics, 5, 653–668, https://doi.org/10.5194/esurf-5-653-2017, 2017a.

Dietze, M., Turowski, J. M., Cook, K. L., and Hovius, N.: Spatiotemporal patterns, triggers and anatomies of seismically detected rockfalls, Earth Surface Dynamics, 5, 757–779, https://doi.org/10.5194/esurf-5-757-2017, 2017b.

Dietze, M., Krautblatter, M., Illien, L., and Hovius, N.: Seismic constraints on rock damaging related to a failing mountain peak: the Hochvo-gel, Allgäu, Earth Surface Processes and Landforms, 46, 417–429, https://doi.org/10.1002/esp.5034, 2021.

Eberhardt, E., Stead, D., and Coggan, J. S.: Numerical analysis of initiation and progressive failure in natural rock slopes—the 1991 Randa
480   rockslide, International Journal of Rock Mechanics and Mining Sciences, 41, 69–87, https://doi.org/10.1016/S1365-1609(03)00076-5, 2004.

Erismann, T. H. and Abele, G.: Dynamics of rockslides and rockfalls, Springer, Berlin and Heidelberg, ISBN 978-3-662-04639-5, https://doi.org/10.1007/978-3-662-04639-5, 2001.

Gischig, V., Preisig, G., and Eberhardt, E.: Numerical Investigation of Seismically Induced Rock Mass Fatigue as a Mechanism
485   Contributing to the Progressive Failure of Deep-Seated Landslides, Rock Mechanics and Rock Engineering, 49, 2457–2478, https://doi.org/10.1007/s00603-015-0821-z, 2016.

Harp, E. L. and Jibson, R. W.: Anomalous Concentrations of Seismically Triggered Rock Falls in Pacoima Canyon: Are They Caused by Highly Susceptible Slopes or Local Amplification of Seismic Shaking?, Bulletin of the Seismological Society of America, 92, 3180–3189, https://doi.org/10.1785/0120010171, 2002.

490   Heckmann, T., Bimböse, M., Krautblatter, M., Haas, F., Becht, M., and Morche, D.: From geotechnical analysis to quantification and mod-elling using LiDAR data: a study on rockfall in the Reintal catchment, Bavarian Alps, Germany, Earth Surface Processes and Landforms, 37, 119–133, https://doi.org/10.1002/esp.2250, 2012.

Helmstetter, A. and Garambois, S.: Seismic monitoring of Séchilienne rockslide (French Alps): Analysis of seismic signals and their corre-lation with rainfalls, Journal of Geophysical Research, 115, https://doi.org/10.1029/2009JF001532, 2010.

495   Hibert, C., Mangeney, A., Grandjean, G., and Shapiro, N. M.: Slope instabilities in Dolomieu crater, Réunion Island: From seismic signals to rockfall characteristics, Journal of Geophysical Research, 116, https://doi.org/10.1029/2011JF002038, 2011.

Hibert, C., Provost, F., Malet, J.-P., Maggi, A., Stumpf, A., and Ferrazzini, V.: Automatic identification of rockfalls and volcano-tectonic earthquakes at the Piton de la Fournaise volcano using a Random Forest algorithm, Journal of Volcanology and Geothermal Research, 340, 130–142, https://doi.org/10.1016/j.jvolgeores.2017.04.015, 2017.

500   Hilger, P., Hermanns, R. L., Czekirda, J., Myhra, K. S., Gosse, J. C., and Etzelmüller, B.: Permafrost as a first order control on long-term rock-slope deformation in (Sub-)Arctic Norway, Quaternary Science Reviews, 251, 106 718, https://doi.org/10.1016/j.quascirev.2020.106718, 2021.

Hutter, P.: Damals im Oberallgäu: Geschichte(n) aus der südlichsten Region Deutschlands, Ed. Limosa, Clenze, 1. aufl. edn., ISBN 978-3-86037-401-6, 2010.

505   IPCC, ed.: Climate Change and Land: an IPCC special report on climate change, desertification, land degradation, sustainable land manage-ment, food security, and greenhouse gas fluxes in terrestrial ecosystems: Shukla, P.R. et al. (eds.), in press, 2019.

Jibson, R. W.: Predicting earthquake-induced landslide displacements using Newmark's sliding block analysis, Transportation Research Record, pp. 9–17, 1993.

Jibson, R. W.: Regression models for estimating coseismic landslide displacement, Engineering Geology, 91, 209–218,
510   https://doi.org/10.1016/j.enggeo.2007.01.013, 2007.

Jibson, R. W., Harp, E. L., and Michael, J. A.: A method for producing digital probabilistic seismic landslide hazard maps, Engineering Geology, 58, 271–289, https://doi.org/10.1016/S0013-7952(00)00039-9, 2000.

Jibson, R. W., Harp, E. L., Schulz, W., and Keefer, D. K.: Large rock avalanches triggered by the M 7.9 Denali Fault, Alaska, earthquake of 3 November 2002, Engineering Geology, 83, 144–160, https://doi.org/10.1016/j.enggeo.2005.06.029, 2006.

25

515 Kemeny, J.: The Time-Dependent Reduction of Sliding Cohesion due to Rock Bridges Along Discontinuities: A Fracture Mechanics Approach, Rock Mechanics and Rock Engineering, 36, 27–38, https://doi.org/10.1007/s00603-002-0032-2, 2003.

Khan, S., van der Meijde, M., van der Werff, H., and Shafique, M.: The impact of topography on seismic amplification during the 2005 Kashmir earthquake, Natural Hazards and Earth System Sciences, 20, 399–411, https://doi.org/10.5194/nhess-20-399-2020, 2020.

Knapp, S., Gilli, A., Anselmetti, F. S., Krautblatter, M., and Hajdas, I.: Multistage Rock–Slope Failures Revealed in Lake Sediments in
520 a Seismically Active Alpine Region (Lake Oeschinen, Switzerland), Journal of Geophysical Research: Earth Surface, 123, 658–677, https://doi.org/10.1029/2017JF004455, 2018.

Krautblatter, M., Funk, D., and Günzel, F. K.: Why permafrost rocks become unstable: a rock–ice–mechanical model in time and space, Earth Surface Processes and Landforms, 38, 876–887, https://doi.org/10.1002/esp.3374, 2013.

Lacasse, S. and Nadim, F.: Landslide Risk Assessment and Mitigation Strategy, in: Landslides – Disaster Risk Reduction, edited by Sassa,
525 K. and Canuti, P., pp. 31–61, Springer Berlin Heidelberg, Berlin, Heidelberg, ISBN 978-3-540-69966-8, https://doi.org/10.1007/978-3-540-69970-5_3, 2009.

Lagarde, S., Dietze, M., Hammer, C., Zeckra, M., Voigtländer, A., Illien, L., Schöpa, A., Hirschberg, J., Burtin, A., Hovius, N., and Turowski, J. M.: Rock slope failure preparation paced by total crack boundary length, Communications Earth & Environment, 4, https://doi.org/10.1038/s43247-023-00851-0, 2023.

530 LaHusen, S. R., Duvall, A. R., Booth, A. M., Grant, A., Mishkin, B. A., Montgomery, D. R., Struble, W., Roering, J. J., and Wartman, J.: Rainfall triggers more deep-seated landslides than Cascadia earthquakes in the Oregon Coast Range, USA, Science advances, 6, https://doi.org/10.1126/sciadv.aba6790, 2020.

Langet, N. and Silverberg, F. M. J.: Automated classification of seismic signals recorded on the Åknes rock slope, Western Norway, using a convolutional neural network, Earth Surface Dynamics, 11, 89–115, https://doi.org/10.5194/esurf-11-89-2023, 2023.

535 Lee, S.-J., Chan, Y.-C., Komatitsch, D., Huang, B.-S., and Tromp, J.: Effects of Realistic Surface Topography on Seismic Ground Motion in the Yangminshan Region of Taiwan Based Upon the Spectral-Element Method and LiDAR DTM, Bulletin of the Seismological Society of America, 99, 681–693, https://doi.org/10.1785/0120080264, 2009a.

Lee, S.-J., Komatitsch, D., Huang, B.-S., and Tromp, J.: Effects of Topography on Seismic-Wave Propagation: An Example from Northern Taiwan, Bulletin of the Seismological Society of America, 99, 314–325, https://doi.org/10.1785/0120080020, 2009b.

540 Lehning, M., Bartelt, P., Brown, B., Russi, T., Stöckli, U., and Zimmerli, M.: Snowpack model calculations for avalanche warning based upon a new network of weather and snow stations, Cold Regions Science and Technology, 30, 145–157, https://doi.org/10.1016/S0165-232X(99)00022-1, 1999.

Leinauer, J.: Collection of R-codes and data for analysis of drivers at the Hochvogel rock slope instability, https://doi.org/10.5281/zenodo.10567098, 2024.

545 Leinauer, J., Jacobs, B., and Krautblatter, M.: Anticipating an imminent large rock slope failure at the Hochvogel (Allgäu Alps), Geomechanics and Tunnelling, 13, 597–603, https://doi.org/10.1002/geot.202000027, 2020.

Leinauer, J., Jacobs, B., and Krautblatter, M.: High alpine geotechnical real time monitoring and early warning at a large imminent rock slope failure (Hochvogel, GER/AUT), IOP Conference Series: Earth and Environmental Science, 833, 012 146, https://doi.org/10.1088/1755-1315/833/1/012146, 2021.

550 Leinauer, J., Weber, S., Cicoira, A., Beutel, J., and Krautblatter, M.: An approach for prospective forecasting of rock slope failure time, Communications Earth & Environment, 4, https://doi.org/10.1038/s43247-023-00909-z, 2023.

Marc, O., Hovius, N., Meunier, P., Gorum, T., and Uchida, T.: A seismologically consistent expression for the total area and volume of earthquake-triggered landsliding, Journal of Geophysical Research: Earth Surface, 121, 640–663, https://doi.org/10.1002/2015JF003732, 2016.

555 Massey, C. I., Olsen, M. J., Wartman, J., Senogles, A., Lukovic, B., Leshchinsky, B. A., Archibald, G., Litchfield, N., van Dissen, R., de Vilder, S., and Holden, C.: Rockfall Activity Rates Before, During and After the 2010/2011 Canterbury Earthquake Sequence, Journal of Geophysical Research: Earth Surface, 127, https://doi.org/10.1029/2021JF006400, 2022.

Meunier, P., Hovius, N., and Haines, A. J.: Regional patterns of earthquake-triggered landslides and their relation to ground motion, Geophysical Research Letters, 34, https://doi.org/10.1029/2007GL031337, 2007.

560 Meunier, P., Hovius, N., and Haines, J. A.: Topographic site effects and the location of earthquake induced landslides, Earth and Planetary Science Letters, 275, 221–232, https://doi.org/10.1016/j.epsl.2008.07.020, 2008.

Meyenfeld, H.: Modellierungen seismisch ausgelöster gravitativer Massenbewegungen für die Schwäbische Alb und den Raum Bonn und Erstellen von Gefahrenhinweiskarten: Dissertation, ULB Bonn, Bonn, 2009.

Miles, S. B. and Keefer, D. K.: Seismic Landslide Hazard for the City of Berkeley, California, U.S. Geological Survey, 565 https://doi.org/10.3133/mf2378, 2001.

Mulas, M., Marnas, M., Ciccarese, G., and Corsini, A.: Sinusoidal wave fit indexing of irreversible displacements for crackmeters monitoring of rockfall areas: test at Pietra di Bismantova (Northern Apennines, Italy), Landslides, 17, 231–240, https://doi.org/10.1007/s10346-019-01248-x, 2020.

Newmark, N. M.: Effects of earthquakes on dams and embankments, Geotechnique, 15, 139–160, 1965.

570 Oswald, P., Strasser, M., Hammerl, C., and Moernaut, J.: Seismic control of large prehistoric rockslides in the Eastern Alps, Nature communications, 12, 1059, https://doi.org/10.1038/s41467-021-21327-9, 2021.

Oswald, P., Strasser, M., Skapski, J., and Moernaut, J.: Magnitude and source area estimations of severe prehistoric earthquakes in the western Austrian Alps, Natural Hazards and Earth System Sciences, 22, 2057–2079, https://doi.org/10.5194/nhess-22-2057-2022, 2022.

Pecoraro, G., Calvello, M., and Piciullo, L.: Monitoring strategies for local landslide early warning systems, Landslides, 16, 213–231, 575 https://doi.org/10.1007/s10346-018-1068-z, 2019.

Petley, D. N.: The evolution of slope failures: mechanisms of rupture propagation, Natural Hazards and Earth System Sciences, 4, 147–152, https://doi.org/10.5194/nhess-4-147-2004, 2004.

Picarelli, L., Lacasse, S., and Ho, K. K. S.: The Impact of Climate Change on Landslide Hazard and Risk, in: Understanding and Reducing Landslide Disaster Risk, edited by Sassa, K., Mikoš, M., Sassa, S., Bobrowsky, P. T., Takara, K., and Dang, K., ICL Con-580 tribution to Landslide Disaster Risk Reduction, pp. 131–141, Springer International Publishing, Cham, ISBN 978-3-030-60195-9, https://doi.org/10.1007/978-3-030-60196-6_6, 2021.

Preisig, G., Eberhardt, E., Smithyman, M., Preh, A., and Bonzanigo, L.: Hydromechanical Rock Mass Fatigue in Deep-Seated Landslides Accompanying Seasonal Variations in Pore Pressures, Rock Mechanics and Rock Engineering, 49, 2333–2351, https://doi.org/10.1007/s00603-016-0912-5, 2016.

585 Provost, F., Hibert, C., and Malet, J.-P.: Automatic classification of endogenous landslide seismicity using the Random Forest supervised classifier, Geophysical Research Letters, 44, 113–120, https://doi.org/10.1002/2016GL070709, 2017.

R Core Team: R: A Language and Environment for Statistical Computing, https://www.R-project.org/, 2023.

Rault, C., Chao, W.-A., Gelis, C., Burtin, A., Chang, J.-M., Marc, O., Lai, T.-S., Wu, Y.-M., Hovius, N., and Meunier, P.: Seismic Response of a Mountain Ridge Prone to Landsliding, Bulletin of the Seismological Society of America, 110, 3004–3020, https://doi.org/10.1785/0120190127, 2020.

Sättele, M., Krautblatter, M., Bründl, M., and Straub, D.: Forecasting rock slope failure: how reliable and effective are warning systems?, Landslides, 13, 737–750, https://doi.org/10.1007/s10346-015-0605-2, 2016.

Scandroglio, R., Stoll, V., and Krautblatter, M.: The driving force of all nature. Modelling water pressure and its stability consequences on alpine bedrock slopes, IOP Conference Series: Earth and Environmental Science, 833, 012 109, https://doi.org/10.1088/1755-1315/833/1/012109, 2021.

SED: Earthquake Catalogue: Swiss Seismological Service, http://www.seismo.ethz.ch/en/research-and-teaching/products-software/earthquake-catalogues/, 2023.

Senfaute, G., Duperret, A., and Lawrence, J. A.: Micro-seismic precursory cracks prior to rock-fall on coastal chalk cliffs: a case study at Mesnil-Val, Normandie, NW France, Natural Hazards and Earth System Sciences, 9, 1625–1641, https://doi.org/10.5194/nhess-9-1625-2009, 2009.

Sepúlveda, S. A., Murphy, W., Jibson, R. W., and Petley, D. N.: Seismically induced rock slope failures resulting from topographic amplification of strong ground motions: The case of Pacoima Canyon, California, Engineering Geology, 80, 336–348, https://doi.org/10.1016/j.enggeo.2005.07.004, 2005.

Stock, G., Collins, B., Santaniello, D., Zimmer, V., Wieczorek, G., and Synder, J.: Historical rock falls in Yosemite National Park, California (1857–2011), Data Series 746, 2013.

USGS: Earthquake Catalogue: US Geological Service, https://earthquake.usgs.gov/earthquakes/search/, 2023.

Voigtländer, A., Leith, K., and Krautblatter, M.: Subcritical Crack Growth and Progressive Failure in Carrara Marble Under Wet and Dry Conditions, Journal of Geophysical Research: Solid Earth, 123, 3780–3798, https://doi.org/10.1029/2017JB014956, 2018.

Weber, S., Beutel, J., Faillettaz, J., Hasler, A., Krautblatter, M., and Vieli, A.: Quantifying irreversible movement in steep, fractured bedrock permafrost on Matterhorn (CH), The Cryosphere, 11, 567–583, https://doi.org/10.5194/tc-11-567-2017, 2017.

Weber, S., Beutel, J., Häusler, M., Geimer, P. R., Fäh, D., and Moore, J. R.: Spectral amplification of ground motion linked to resonance of large-scale mountain landforms, Earth and Planetary Science Letters, 578, 117 295, https://doi.org/10.1016/j.epsl.2021.117295, 2022.

Wenner, M., Hibert, C., van Herwijnen, A., Meier, L., and Walter, F.: Near-real-time automated classification of seismic signals of slope failures with continuous random forests, Natural Hazards and Earth System Sciences, 21, 339–361, https://doi.org/10.5194/nhess-21-339-2021, 2021.

Wieczorek, G.: Landslide triggering mechanisms, in: Landslides - investigation and mitigation, edited by Turner, A. and Schuster, R., pp. 76–90, National Academy Press, 1996.

Wilson, R. C. and Keefer, D. K.: Predicting Areal Limits of Earthquake-Induced Landsliding, in: Evaluating Earthquake Hazards in the Los Angeles Region - An Earth-Science Perspective, edited by U.S. Geological Survey, pp. 316–345, USGS, 1985.

Wyllie, D. C. and Mah, C. W.: Rock slope engineering: Civil and mining, Spon Press, New York, NY, repr., 4. ed. edn., ISBN 978-0-415-28001-3, http://www.loc.gov/catdir/enhancements/fy0650/2003014937-d.html, 2004.